ADVANCED MATERIALS
www.advmat.de

Synergistic Bulk and Surface Engineering for Expeditious and Durable Reversible Protonic Ceramic Electrochemical Cells Air Electrode

Xi Chen, Na Yu, Yufei Song, Tong Liu, Hengyue Xu, Daqin Guan, Zheng Li, Wei-Hsiang Huang, Zongping Shao, Francesco Ciucci, and Meng Ni**

Reversible protonic ceramic electrochemical cells (R-PCECs) offer the potential for high-efficiency power generation and green hydrogen production at intermediate temperatures. However, the commercial viability of R-PCECs is hampered by the sluggish kinetics of the oxygen reduction reaction (ORR) and oxygen evolution reaction (OER) within conventional air electrodes operating at reduced temperatures. To address this challenge, this work introduces a novel approach based on the simultaneous optimization of bulk-phase metal-oxygen bonds and in-situ formation of a metal oxide nano-catalyst surface modification. This strategy is designed to expedite the ORR/OER electrocatalytic activity of air electrodes exhibiting triple (O^{2-}, H^{+}, e^{-}) conductivity. Specifically, this engineered air electrode nanocomposite-Ba($Co_{0.4}Fe_{0.4}Zr_{0.1}Y_{0.1}$)$_{0.95}Ni_{0.05}F_{0.1}O_{2.9-\delta}$ demonstrates remarkable ORR/OER catalytic activity and exceptional durability in R-PCECs. This is evidenced by significantly improved peak power density from 626 to 996 mW cm^{-2} and highly stable reversibility over a 100-h cycling period. This research offers a rational design strategy to achieve high-performance R-PCEC air electrodes with superior operational activity and stability for efficient and sustainable energy conversion and storage.

1. Introduction

With the constraints imposed by fossil fuels and the undesirable consequences of anthropogenic greenhouse gas emissions, there is a growing interest in developing highly efficient, sustainable, and environmentally friendly energy power plants for carbon-free energy generation.[1–3] Among these, reversible solid oxide cells (R-SOCs), capable of functioning reversibly as both fuel cells (FCs) and electrolysis cells (ECs), have emerged as promising candidates for energy conversion (in FC mode) and storage (in EC mode) without the inherent drawbacks of intermittency and variability for the traditional renewable energy systems.[4–6] Additionally, they offer other significant advantages, including high energy conversion efficiency, low emissions, quiet operation, and fuel flexibility for on-demand electric power production.[7] Nevertheless, compared to conventional oxygen ion-conducting R-SOCs operating at intermediate-high temperatures (600–1000 °C), the reversible protonic ceramic electrochemical cells (R-PCECs) can efficiently operate at reduced temperatures (350–650 °C) due to the rapid proton transport and lower proton-migration activation energy (0.4–0.6 eV), which extends the cells' lifespan and reduces production and operation costs.[8,9]

R-PCECs hold significant potential, but their large-scale adoption depends on developing air electrodes that support efficient, stable oxygen reduction reaction (ORR) and oxygen evolution

X. Chen, N. Yu, T. Liu, D. Guan, Z. Li, M. Ni
Department of Building and Real Estate
Research Institute for Sustainable Urban Development (RISUD) and Research Institute for Smart Energy (RISE)
The Hong Kong Polytechnic University
Hung Hom, Kowloon, Hong Kong 999077, China
E-mail: meng.ni@polyu.edu.hk

The ORCID identification number(s) for the author(s) of this article can be found under https://doi.org/10.1002/adma.202403998

DOI: 10.1002/adma.202403998

Y. Song, F. Ciucci
Department of Mechanical and Aerospace Engineering
The Hong Kong University of Science and Technology
Clear Water Bay, Hong Kong 999077, China
E-mail: francesco.ciucci@uni-bayreuth.de

H. Xu
Institute of Biopharmaceutical and Health Engineering
Tsinghua Shenzhen International Graduate School
Tsinghua University
Shenzhen 518055, China

W.-H. Huang
National Synchrotron Radiation Research Center (NSRRC)
Hsinchu 30076, Taiwan

Z. Shao
WA School of Mines: Minerals Energy and Chemical Engineering (WASM-MECE)
Curtin University
Perth, WA 6845, Australia

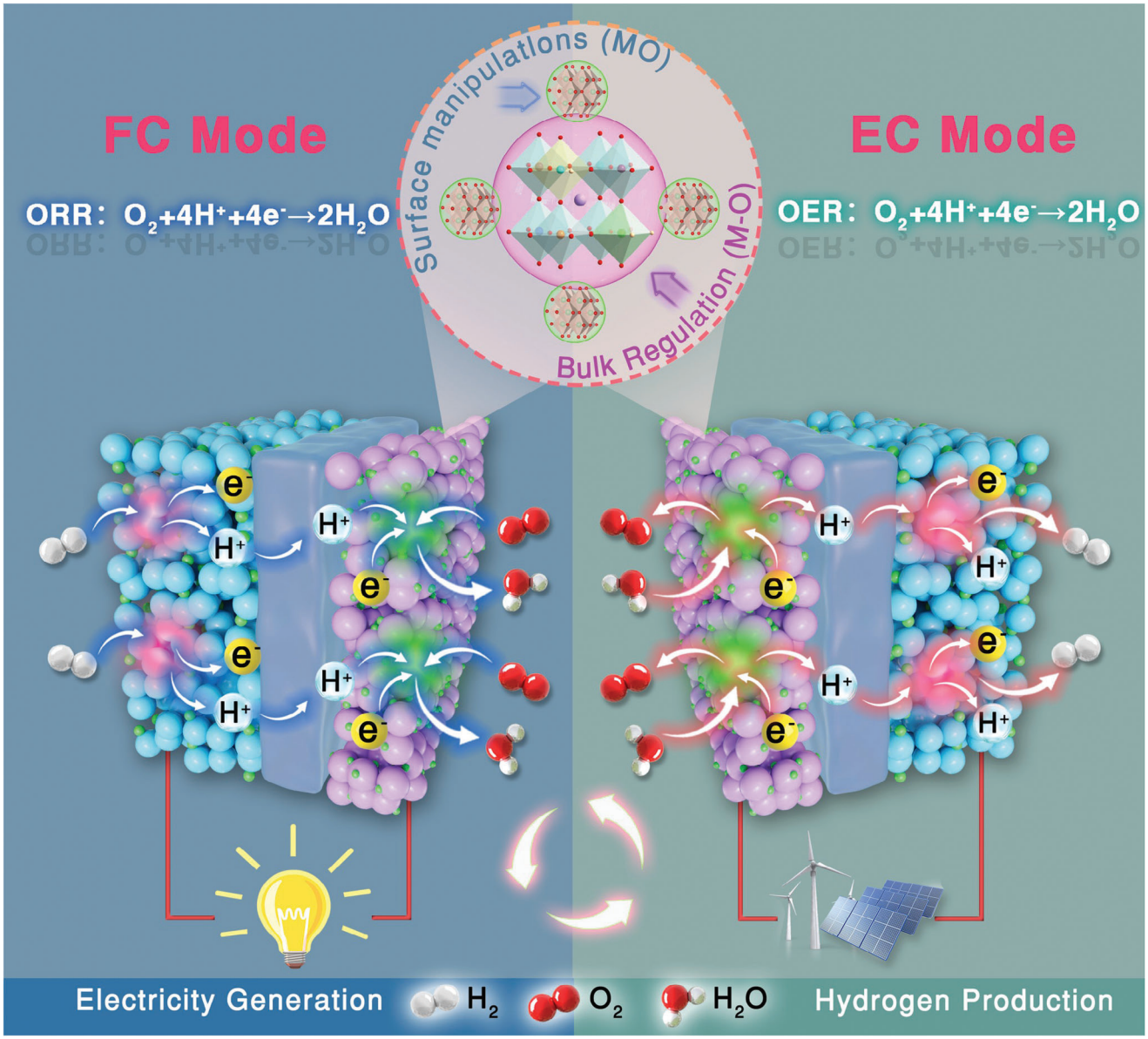

Figure 1. Schematic diagram of R-PCEC in fuel cell (FC) and electrolysis cell (EC) operation modes along with the bulk and in-situ surface modification strategy for air electrode.

reaction (OER) at lower operating temperatures while switching seamlessly between FC and EC modes. Although many air electrodes have been explored in recent decades, achieving sufficient electrochemical performance remains a significant challenge. Therefore, it is imperative to develop effective strategies to enhance the ORR/OER electrode kinetics and durability to accelerate the development of R-PCECs.

Considering that under actual operating conditions, the ORR and OER in the R-PCEC air electrodes primarily involve the following sub-steps: adsorption/desorption of oxygen/water (steam) on the electrode surface; the reduction of active oxygen/ the oxidization of water (steam) to corresponding active ions (O^{2-}, H^+/ hydroxyl); the surface and bulk transport of active ions; and the generation of water (steam) /oxygen with the participation of electrons (**Figure 1**). It is foreseeable that the air electrodes with highly efficient O^{2-}, H^+, e^- (triple-conducting oxide, TCO) transfer capabilities, coupled with activated surface sites, hold promise as ideal dual-functional catalysts for R-PCECs. This potential arises from the significantly enhanced surface and bulk ion generation and transport capabilities, extending the effective three-phase boundaries (TPBs, active reaction sites) and accelerating the electrode reaction kinetics.

Currently, as a prototypic perovskite TCO, $BaCo_{0.4}Fe_{0.4}Zr_{0.1}Y_{0.1}O_{3-\delta}$ (BCFZY) is widely applied in proton-conducting fuel cells as air electrode material since it possesses convincing ORR catalytic activity.[10] Unfortunately, when it is directly employed as the air electrode for R-PCECs, the electrochemical catalytic activity significantly diminishes due to the lower capability

of oxygen ion/proton formation and transport, particularly in humid conditions.[11] Therefore, extensive efforts have been devoted to developing new, effective, high triple-conducting air electrodes. Recent studies have demonstrated the efficacy of partial substituting A-site of perovskite TCO materials with high-basicity elements to adjust the alkalinity and carrier concentration of oxides. Building upon this, a specific instance of this approach involved the partial potassium (K) doping to create $Ba_{0.9}K_{0.1}Co_{0.4}Fe_{0.4}Zr_{0.2}O_{3-\delta}$,[12] $Ba_{0.4}K_{0.1}Sr_{0.5}Co_{0.8}Fe_{0.2}O_{3-\delta}$,[13] and $Sr_{1.75}K_{0.25}Fe_{1.5}Mo_{0.5}O_{6-\delta}$[14] air electrodes. Additionally, a systematic exploration was conducted for different A-site element substitutions in the double perovskite material ($LnBa_{0.5}Sr_{0.5}Co_{1.5}Fe_{0.5}O_{5+\delta}$ (LnBSCF, Ln = Pr, Nd, and Gd)).[1] All modified materials showed lower proton migration barrier and increased proton defect concentration. Several works have studied the effectiveness of partial B-site substitution in single-phase TCOs, including P ($Ba_{0.5}Sr_{0.5}(Co_{0.8}Fe_{0.2})_{0.95}P_{0.05}O_{3-\delta}$),[15] Mg ($Ba(Co_{0.4}Fe_{0.4}Zr_{0.1}Y_{0.1})_{0.95}Mg_{0.05}O_{3-\delta}$),[16] and Cs ($PrBa_{0.9}Cs_{0.1}Co_2O_{5+\delta}$)[17] electrodes, enhancing the triple conductivity. Remarkably, whether the modification is carried out at the A-site or B-site of conventional perovskite TCO materials, these methodologies are based on regulating the metal-oxygen (M—O) chemical bonds within the lattice which affect the Lewis acidity and defects (oxygen vacancies and proton defects) concentration and mobility. This strategy has been validated by the density functional theory calculations and experiments.[18–20] Additionally, directly modulating the anions in perovskite oxides is another effective strategy for fine-tuning the M—O chemical bonds within their lattice.[21] This method not only maintains the structural stability through A-site metal cations but also preserves the catalytic attributes of B-site metal cations critical for electrochemical reactions, holding significant promise for designing catalyst materials that are both highly efficient and stable. Notably, considering the electronegativity of fluorine (χ = 3.98) surpasses that of oxygen (χ = 3.44), and the valence electron density of oxygen is lower than that of fluorine, the introduction of fluorine is anticipated to reduce the coulombic forces between B-site metallic ions and oxygen ions.[22] Consequently, this adjustment weakens the M—O chemical bonds, thus improving the generation and migration capabilities of active carriers.

In addition to modifying the main phase, surface regulation has also proven to be a highly efficient method for enhancing the catalytic activity of air electrodes.[23] For instance, the incorporation of the heteroatom boron onto the surface of $Pr_4Ni_3O_{10+\delta}$ through mechanical mixing has been demonstrated to enhance the concentration of surface Brønsted acid (-OH), thereby improving its surface electrocatalytic activity.[24] Additionally, the introduction of nano-catalysts through impregnation, such as infiltrating $BaCoO_{3-\delta}$ on the LSCF surface,[25] coating $Pr_{0.1}Ce_{0.9}O_{2+\delta}$ on the $PrBaCo_2O_{5+\delta}$ surface,[26] and dropping an efficient catalyst $PrNi_{0.5}Co_{0.5}O_{3-\delta}$ on the surface of $BaCe_{0.5}Pr_{0.3}Y_{0.2}O_{3-\delta}$,[27] has exhibited enhanced ORR/OER electrocatalytic activity in R-PCEC air electrodes. Despite these achievements, the challenges of these approaches include the electrodes' uncontrollable appearance and the associated time-consuming and labor-intensive preparation processes. Nowadays, a new focus in air electrode development centers on creating stabilized materials through in situ formations/exsolution of active nanoparticles (NPs).[28] Illustrative examples involve the in situ formation of $Gd_xCo_yO_{3-\delta}$ NPs in a double perovskite $Ba_{0.8}Gd_{0.8-x}Pr_{0.4}Co_{2-y}O_{5+\delta}$,[29] in situ exsolved $BaCoO_{3-\delta}$ nanoparticles on the surface of $PrBa_{0.8}Ca_{0.2}Co_2O_{5+\delta}$,[30] and in situ generation of $BaCeO_3$ and CeO_2 double phases on the surface of $PrBa_{0.8}Ca_{0.2}Fe_{1.8}Ce_{0.2}O_{6-\delta}$.[31] Additionally, the in-situ generation of metal oxide nanoparticles (MO) on the electrode material surface has demonstrated enhanced surface reaction activity. More importantly, these nanoparticles resist reverting to the main phase structure under oxidative conditions, thereby avoiding the loss of catalytic activity, notable examples include NiO nanoparticles.[32,33]

Therefore, it is essential to develop an effective strategy that can simultaneously achieve coordinated improvements in both bulk and surface properties. Herein, we propose an effective strategy aimed at weakening the M—O bonds within the bulk phase, while concurrently facilitating the in-situ generation of MO nanoparticles on the surface. This approach is introduced to synergistically enhance both the bulk ionic transport and surface electrocatalytic properties of TCO air electrode materials. As a result of these modifications, the targeted air electrode exhibits high-efficiency bulk O^{2-}/H^+ transport paths and significantly improved rates of O^{2-}/H^+ migration, along with enhanced surface exchange kinetics. The designed air electrode nanocomposite-$Ba(Co_{0.4}Fe_{0.4}Zr_{0.1}Y_{0.1})_{0.95}Ni_{0.05}F_{0.1}O_{2.9-\delta}$ (N-BCFZYNF) presents significantly improved ORR/OER catalytic activity in R-PCECs with favorable reversible operational stability.

2. Results and Discussion

To identify the effect of these introduced different ions substituted into the B-site and O-site of BCFZY, the room temperature X-ray diffraction (XRD) patterns of the parent BCFZY and the targeted N-BCFZYNF powders were observed, as shown in **Figure 2**a. The as-obtained BCFZY showed a single-phase perovskite structure without any impurity phases, while the synthesized N-BCFZYNF sample exhibited a major perovskite phase and a minor NiO phase. This phenomenon may be attributed to the introduction of fluorine (F), an element with a higher electronegativity than oxygen (O), weakening of the M—O bonds within the modified material lattice. This facilitates the selective precipitation of Ni—O (with lower binding energy) from the parent material during the high-temperature treatment process.[34,35] Additionally, the higher diffraction angle of N-BCFZYNF in the enlarged XRD patterns from 36° to 45°, indicates a contraction in its lattice size compared to the BCFZY-based lattice. Considering the larger ionic radius of Ni^{2+} (0.69 Å) in comparison to other B-site metal ions in the host perovskite lattice, coupled with the fact that the ionic radius of F^- (1.33 Å) is smaller than that of O^{2-} (1.40 Å),[16,21] it is highly plausible that, during the synthesis process, fluorine has successfully incorporated into the lattice, while nickel may have been limited in its incorporation. This observation partially accounts for forming a minor amount of NiO in the N-BCFZYNF sample. Additionally, the Rietveld refinement of XRD data of the modified N-BCFZYNF sample was conducted to determine the degree of nickel exsolution, as presented in Figure 2b. A visual representation of the NiO content could be estimated at 1.0%, implying that a significant portion of Ni precipitates from the host phase. On the other hand,

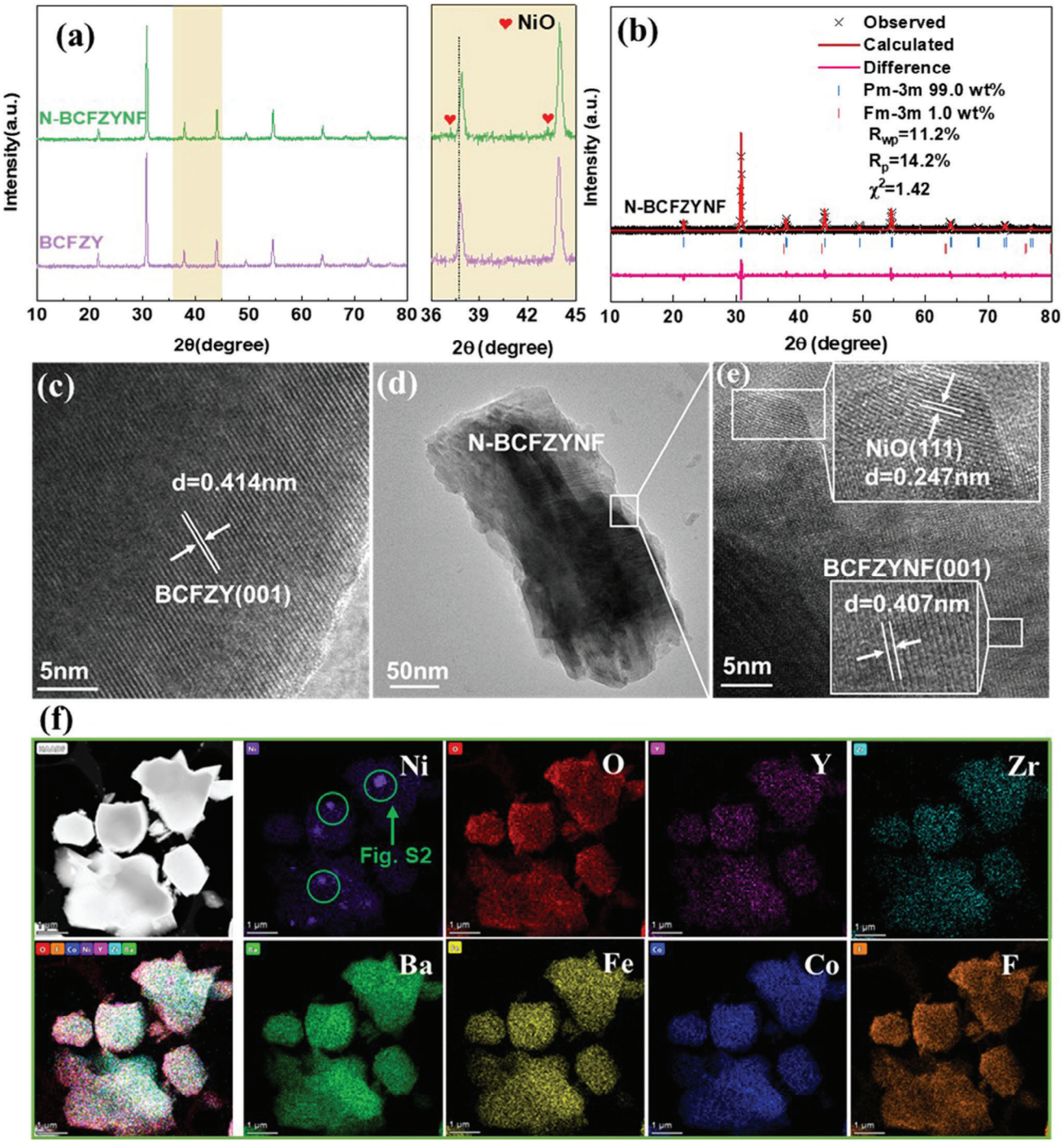

Figure 2. a) The RT-XRD patterns of BCFZY and N-BCFZYNF with a partial enlargement; b) The XRD Rietveld refinement profiles of N-BCFZYNF with two phases; HR-TEM images of the c) BCFZY, d,e) N-BCFZYNF samples; f) The elements distribution of N-BCFZYNF sample.

the theoretical content would amount to 1.5% if Ni ions were to exclusively manifest as NiO on the material surface according to the stoichiometry of the target material, which indicates that Ni did not in-situ precipitate entirely from the lattice but rather selectively precipitate on the surface. Moreover, as compared with the corresponding Rietveld result of parent BCFZY shown in Figure S1, Supporting Information, the N-BCFZYNF oxide exhibited a smaller lattice size while both samples show a cubic structure with space group Pm-3m, which further keeps in line with the XRD patterns exhibited in Figure 2a.

The formation of the two phases of oxide by the introduction of F and Ni was further supported by high-resolution transmission electron microscopy (HR-TEM) images, as shown in Figure 2c–e. The crystalline fringes with the corresponding d-spacing (001

lattice plane) were estimated to be 4.14 Å for the BCFZY sample (Figure 2c). However, the same d-spacing value for the N-BCFZYNF sample was determined to be 4.07 Å (Figure 2e) through the enlargement part of the particle shown in Figure 2d, which intimately agrees with the Rietveld results and the shifted direction of the diffraction peaks. Moreover, Figure 2e showed another diffraction planes with 2.47 Å for the 111-lattice plane of NiO, from which it is also obvious that these two phases were connected well. Meanwhile, the energy dispersive spectroscopy (EDS) mapping results in Figure 2f displayed that Ni aggregated while other metals were distributed uniformly in the single grain, which could be found more clearly in Figure S2, Supporting Information. On the contrary, as shown in Figure S3, Supporting Information, BCFZY has a pure perovskite oxide phase without detectable impurities; all elements were uniformly distributed without obvious segregation. The anion element (F, O) also displayed a similar uniform distribution, indicating the successful incorporation of F into the oxygen site as targeted. These results highly demonstrated the existence of nanoscale NiO particles in the perovskite oxide and the anion dopants were well incorporated into the lattice for the designed N-BCFZYNF sample.

Ideal air electrode functional material for R-PCECs requires high ORR/OER catalytic performance, which is strongly associated with the intrinsic oxygen properties and the oxidation state of the transition metals at B-site of perovskite oxides.[20,33] Therefore, a detailed investigation has been schematically conducted to understand the necessary modifications of conventional air electrodes and the chemical characteristics of oxygen and B-site transition metal cations exhibited by the target air electrode. **Figure 3a** exemplifies the mechanism of substituting F and Ni elements into the parent oxide's O-site and B-site to generate highly active metal-oxygen bonds (M—O) and enable nanoscale metal-oxide (MO) catalysis.[36] To further elucidate the impact on the oxidation state of B-site transition cations, X-ray absorption fine structure (XAFS) was used to compare the valence states of Co and Fe in the bulk phases of BCFZY and N-BCFZYNF. The X-ray absorption near edge (K-edge) structure (XANES) results (Figure 3b,c) reveal a slightly higher valence state of Co in the N-BCFZYNF sample compared to BCFZY, whereas the valence of Fe is nearly constant. Given that the B-site dopant Ni introduced into the lattice primarily exists as a second-phase MO, the observed variations in the valence states are most likely attributed to the introduction of F anions. In fact, besides forming bonds with metals by substituting lattice oxygen sites, F anions may partially occupy oxygen vacancies, increasing the metal valence state. Similar experimental results have also been reported in other studies.[37,38]

As discussed above, the intrinsic oxygen chemical bonds also contribute a lot in achieving outstanding ORR/OER catalytic performance. Considering the importance of oxygen vacancies concentration in air electrode materials, thermogravimetric (TG) analysis was carried out to determine the oxygen non-stoichiometry (δ) of the samples. TG curves in Figure 3d reveal more pronounced weight loss for N-BCFZYNF compared to BCFZY sample within the elevated temperature range of 100 to 1000 °C (solid line). Specifically, the weight loss for BCFZY is 1.7%, while that of N-BCFZYNF is 2.0%. Based on the molecular weights derived from their respective chemical formulas, the 0.3% weight loss difference implies a deviation in the delta of 0.1 of oxygen. Increased oxygen vacancies in the modified material suggest greater crystal oxygen activation at intermediate temperatures. This activation aids oxygen adsorption, oxygen ion generation, and bulk-phase conduction, thus accelerating oxygen kinetics and facilitating the ORR/OER electrochemical processes.[39] Further analysis via O_2-TPD (Temperature Programmed Desorption) supports these findings. This technique evaluates the oxygen desorption properties from 50 to 800 °C (Figure 3e). As the temperature increases, the active cations in the perovskite oxide undergo thermal reduction, leading to a decrease in their oxidation state, with oxygen being simultaneously released. Additionally, the lower initial desorption temperature of N-BCCFZYNF (303.9 °C) compared to BCFZY (323.1 °C) indicates faster surface oxygen exchange kinetics and migration rate within the perovskite lattice. O1s XPS spectra (Figure 3f) offer additional insights; the binding energies of lattice oxygen (O^{2-}) were measured at 528.37 eV and 528.67 eV for BCFZY and N-BCFZYNF samples, respectively. This increase in N-BCFZYNF is likely ascribed to the presence of F^-, which reduces the valence electron density of lattice oxygen. This weakens the chemical bonds between A- or B-site metal cations and oxygen ions (M—O), rendering the lattice oxygen more active. These findings align with the TG and O_2-TPD results.[21,40] Moreover, N-BCFZYNF exhibits a discernibly higher concentration of oxygen species originating from bound water under identical conditions. This suggests significantly enhanced capacity for water and proton uptake, potentially boosting R-PCEC air electrode electrochemical reaction kinetics. In short, the results preliminarily indicate that the modified material creates a more favorable intrinsic oxygen chemical environment for oxygen-involved R-PCEC air electrode reaction processes, potentially leading to enhanced catalytic activity.

To validate the suitability of the improved air electrode material as a superior electrocatalyst for oxygen catalysis, both samples were assembled into $Sm_{0.2}Ce_{0.8}O_{1.9}$ (SDC) electrolyte-supported symmetrical cells as the air electrode. The electrocatalytic performance was assessed through area-specific resistance (ASR) values determined by electrochemical impedance spectroscopy (EIS). As shown in Figure 3g, N-BCFZYNF had a lower ASR value (0.085 Ω cm^2) compared to BCFZY (0.12 Ω cm^2) when operated at 600 °C in dry air. Clearly, the improved N-BCFZYNF holds a much better oxygen catalysis activity under the same conditions, which is strongly associated with the enhanced state of the intrinsic oxygen chemical environment as well as the oxidation state of the B-site cations, as analyzed previously. Furthermore, the Arrhenius plots of the ASR values as a function of the temperature range from 650 to 450 °C are shown in Figure 3h and Table S2, Supporting Information. The N-BCFZYNF shows the lowest ASR values, indicating the best ORR catalytic performance. These results affirm that the active M—O bonds through the incorporation of F^- and the surface modification with MO nanoparticles through incorporation of Ni^{2+} is a highly effective strategy for enhancing the ORR catalytical performance of the R-PCEC air electrode.

Exceptional triple conductivity (e^-, O^{2-}, H^+) capabilities are critical for R-PCEC's air electrode to achieve favorable ORR/OER catalytic performance at intermediate temperatures. To explore the e^- migration prosperity in BCFZY and N-BCFZYNF, the electrical conductivities measurements between 350 and 750 °C in wet air were conducted (**Figure 4a**). Both samples displayed

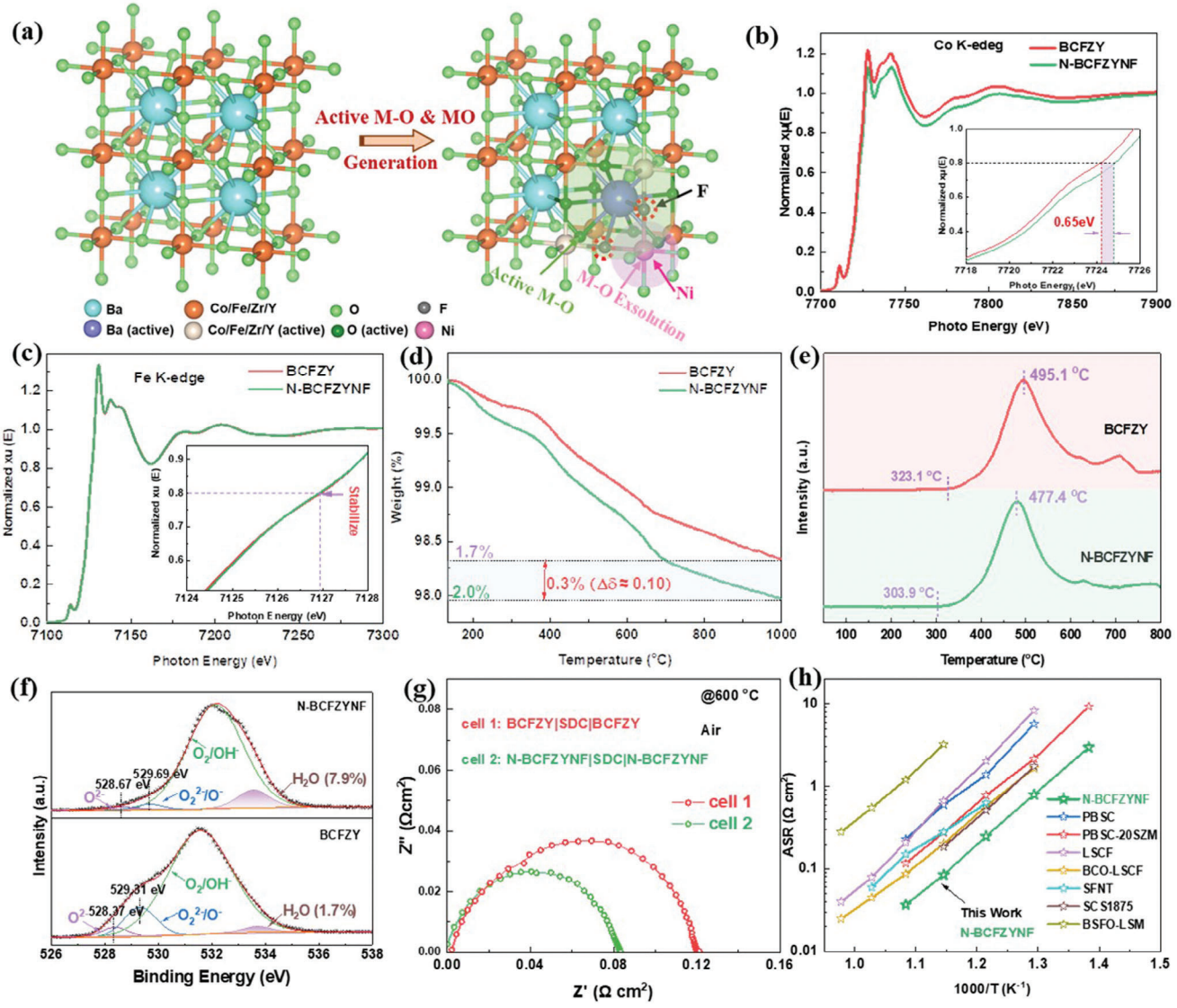

Figure 3. a) Schematic diagram of substituting the O-site and B-site of the parent perovskite oxide with F and Ni elements to generate highly active M—O bonds and MO nanoscale phase. The comparison of BCFZY and modified N-BCFZYNF samples: b) the spectra of Co K-edge XAFS and c) Fe K-edge XAFS plots for these two samples; d) TG curves recorded at the temperature range of 100–1000 °C in dry air; e) O_2 -TPD profiles between 50 and 800 °C; f) the XPS spectra of O-1s; g) the typic Nyquist plots of SDC-electrolyte supported cell at 600 °C in dry air; h) Arrhenius plots of the ASRs of the SDC-supported symmetrical cell as a function of temperatures in dry air.

increasing electrical conductivity with rising temperature, which keeps in line with the p-type semiconducting behavior. Exactly, the BCFZY exhibited values ranging from 1.86 to 1.07 S cm^{-1}, whereas the N-BCFZYNF demonstrated values of 1.51 and 0.97 S cm^{-1}, respectively. The higher conductivities for BCFZY compared to N-BCFZYNF mainly resulting from the higher concentration of the oxygen vacancies and the interface regions between the main cubic phase and NiO phase, since they can act as the scattering centers or random traps for electrons.[41–43]

One key factor influencing the ORR/OER kinetics of air electrode material with triple conductivity is the rate of oxygen incorporation rate. Herein, the ECR measurement was used to investigate the oxygen surface exchange kinetics by switching the operating atmosphere's oxygen partial pressure from 0.21 to 0.10 atm and recording the changing conductivity values.[44,45] These ECR response profiles provided valuable insights into the chemical surface oxygen exchange (k_{chem}) process. The normalizing conductivity relaxation curves were shown in Figures 4b and S4, Supporting Information, and the specific k_{chem} values in temperature ranging from 650 to 450 °C were shown in Figure 4c. The modified N-BCFZYNF sample exhibits a shorter relaxation time compared to BCFZY under the same conditions. For instance, as shown in Figure 4b, the relaxation time for BCFZY is 453 s at 600 °C, while that of N-BCFZYNF is significantly shortened to only 120 s, which preliminarily implies an accelerated oxygen incorporation kinetic. Furthermore, it is confirmed by the larger k_{chem} values obtained from fitting the normalized conductivity relaxation curves. Specifically, the k_{chem} value of BCFZY at 600 °C

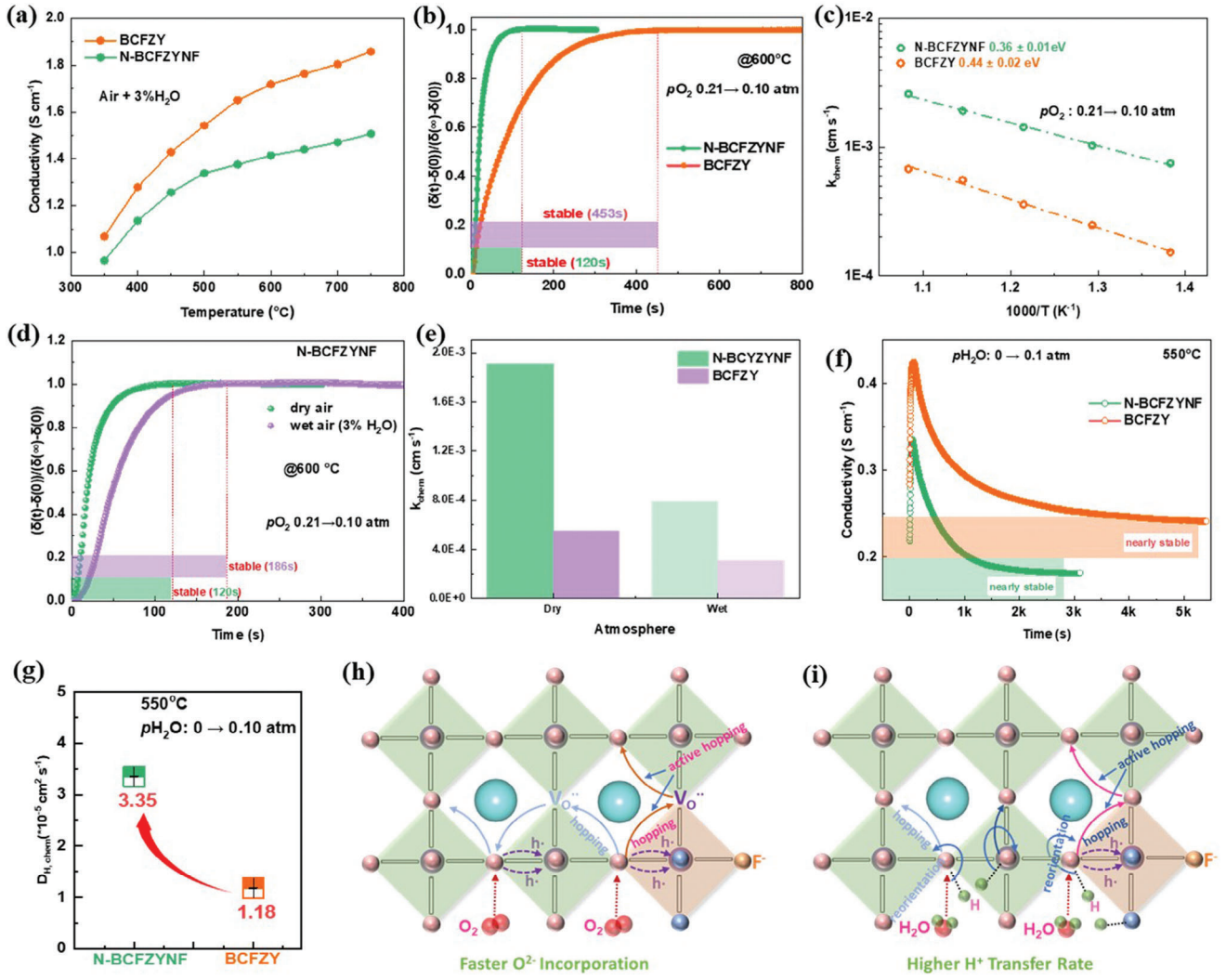

Figure 4. The triple conductivity (e^-, O^{2-}, H^+) properties for BCFZY and N-BCFZYNF samples: a) the electronic conductivity at 350–750 °C in wet air; b) the ECR responses curves when switching oxygen partial pressure in dry air at 600 °C; c) the fitted k_{chem} values from 450 to 650 °C and their corresponding Arrhenius plots; d) the comparison ECR response profiles of N-BCFZYNF in dry and wet air; e) the summarized k_{chem} values obtained from the different ECR process in dry and wet air; f) the typic ECR response profiles when switching the atmospheres from dry to $pH_2O = 0.10$ atm at 550 °C; g) the comparison of fitted $D_{H,chem}$ values shown in (f); schematic diagrams of h) faster O^{2-} incorporation kinetics and i) higher H^+ migration rate properties for the designed N-BCFZYNF sample.

was fitted to be 5.53×10^{-4} cm s^{-1}, while that indicator up to 1.91×10^{-3} cm s^{-1} after modification (Figure 4c). Additionally, the activation energy value of k_{chem} values based on operating temperature for N-BCFZYNF (0.36 eV) was lower compared with BCFZY (0.44 eV), confirming that the surface generation and migration of O^{2-} were facilitated and thus prompting the typical ORR/OER steps.

Considering the actual operating atmosphere of R-PCECs' air electrode is humid air, exploring of the oxygen surface exchange kinetic characteristics in wet air is also essential. Figure 4d illustrates the ECR response curves of the N-BCFZYNF sample in both dry and humid air environment. It can be visually observed that the relaxation time significantly increases in humid conditions, from an initial 120 s to 186 s; a similar trend was also observed in the BCFZY sample (Figure S5, Supporting Information). As previously analyzed, a longer relaxation time may indicate the sluggish oxygen ion introduction and migration processes. This is further validated by the k_{chem} values at 600 °C, with results shown in Figure 4e. The k_{chem} values of the N-BCFZYNF sample decrease from 1.91×10^{-3} to 7.91×10^{-4} cm s^{-1}, and a comparable reduction also occurred for the BCFZY sample. However, it is noteworthy that the introduction of Ni and F into the BCFZY lattice results in significantly higher k_{chem} compared to the parent sample, suggesting a more robust oxygen ion migration capability of the targeted N-BCFZYNF sample even in the humid atmosphere. These results further demonstrate that introducing F into the BCFZY lattice and the presence of Ni oxide on the surface can significantly enhance the generation and migration of oxygen ions, providing possibilities for higher ORR/OER catalytic activity.

Beyond the stronger oxygen mobile ability, the fast proton migration capability is also essential in attaining favorable ORR/OER catalytic performance. Herein, a feasible way by uplifting the H_2O partial pressure from dry (0 atm) to wet (0.1 atm) in the testing atmosphere was applied, and then the values of chemical diffusion coefficient of protons ($D_{H,chem}$) were determined from this prudent ECR responses to assess the protons transfer rate.[46] The typic ECR profiles were shown in Figure 4f, it can be clearly seen that the electrical conductance of BCFZY sample first experienced a short period of rising, and then subsequently decreased until reaching a steady state, similar curves trend was also observed for N-BCFZYNF sample. These interesting non-monotonic relaxation curves can be explained by the phenomenon that all the carriers (oxygen vacancies, holes, and proton defects) would redistribute accompanied by the proton transfer step.[18,46,47] Moreover, compared to the BCFZY material, the modified N-BCFZYNF air electrode material exhibits a faster response to changes in external humidity, with a significantly shortened relaxation time. This preliminarily confirms its enhanced proton transport capability. Additionally, based on the normalized conductivity profiles of the air electrode samples at 550 °C, different $D_{H,chem}$ values were obtained and summarized in Figure 4g. The N-BCFZYNF sample demonstrates a higher $D_{H,chem}$ value of 3.35×10^{-5} cm^2 s^{-1}, nearly three times more than that of BCFZY sample (1.18×10^{-5} cm^2 s^{-1}) under the same test conditions. These results further affirm the pronounced proton bulk transport capability of the N-BCFZYNF sample activated by M—O bonds.

In general, these results demonstrated that the vital oxygen incorporation and proton mobility ability of the R-PCECs' air electrode were significantly improved after incorporating F into the perovskite oxide lattice to activate the M—O chemical bonds and decorating the MO nanoscale catalyst on the parent oxide surface. The mechanism of this promotion is schematically shown in Figure 4h,i from the aspect of lattice structure.[19,48,49] Benefiting from the altered oxidative environment within the material after modification, as well as the enhanced catalytic activity on the material surface, there is a noticeable acceleration in both surface oxygen exchange and bulk-phase oxygen transport processes, which manifests as a faster generation and migration of oxygen ions (even under humid conditions). Additionally, owing primarily to the activation of M—O bonds resulting from the replacement of lattice oxygen with more electronegative F anions in the bulk phase, and the lower Coulombic attraction between lattice oxygen and proton defects, the modified material exhibits enhanced hydration capability and proton migration processes. Combined with these enhancement factors, it is foreseeable that the surface modification fluorinated BCFZY air electrode may holds better ORR/OER catalytic performance and could be employed as an ideal air electrode in R-PCECs.

The electrocatalytic performance of the air electrodes was systematically investigated by assembling them in symmetrical cells with the configuration of (N)BCFZY(NF)|BZCYYb|(N)BCFZY(NF). Here, the specific composition of the BZCYYb electrolyte used here is $BaZr_{0.1}Ce_{0.7}Y_{0.1}Yb_{0.1}O_{3-\delta}$, more details were provided in the experimental section of the Supporting Information. The detailed electrochemical reaction steps, illustrated in **Figure 5a**, provide a deeper insight into the mechanisms of the ORR/OER processes, simultaneously aiding in the elucidation of the specific factors contributing to the enhancement of electrode kinetics. The typic EIS was applied to evaluate the electrocatalytic activity, with the recorded Nyquist plots between 450 and 650 °C being shown in Figure S6, Supporting Information. It could be found that the N-BCFZYNF exhibited a lower ASR value compared to the raw BCFZY at the same operating temperature in wet air. Specifically, as shown in Figure 5b, the ASR value for BCFZY electrode is determined to be 0.264 Ω cm^2 at 600 °C, whereas that for N-BCFZYNF is only 0.165 Ω cm^2, indicating the better catalytic performance was achieved after targeted modification. To get further intuitive insights into this noticeable improvement, the distribution of relaxation time (DRT) technology[50] was conducted by deconvoluting the corresponding EIS response to separate the overlapping electrode processes, with the results displayed in Figure S7, Supporting Information. Three main characteristic peaks were observed in the DRT plots denoted as three different segments according to the located frequency range: low frequency P1 (LF, $< 10^0$ Hz), intermediate frequency P2 (IF, 10^0–10^2 Hz), and high frequency P3 (HF, $>10^2$ Hz). Referring the previously reported DRT analysis results and their located peak patterns related to R-PCEC air electrode, as well as the detailed ORR/OER processes involved shown in Figure 5a, these can be assigned to the gas (O_2/steam) diffusion (P1), surface exchange and/or ions (H^+/O^{2-}) bulk migration (P2, Padd1 and Padd2), and ions/charges transfer in the interface between the electrolyte and electrode at three-phase boundaries (P3). Based on these illustrated results, the accelerated air electrode kinetic for N-BCFZYNF is mainly due to the expeditious sub-steps of surface exchange and ions bulk diffusion since the intermediate frequency peaks (P2, Padd1 and Padd2) reduced significantly compared to the pristine BCFZY, which stems from two key factors: the enhanced surface exchange rate facilitated by the in-situ generation of NiO nanoparticles and the attenuated bulk M—O chemical bonds. In addition, the Arrhenius plots of ASR values as a function of temperature were calculated to compare with other reported high-temperature air electrodes based on proton-conducting BZCYYb electrolyte-supported cells in wet air, with the results summarized in Figure 5c and Table S3, Supporting Information. The N-BCFZYNF electrode still exhibited the smallest ASR values with a significantly reduced electrode reaction activation energy (Ea), at only 1.16 eV, indicating the best catalytic activity for the air electrode reactions was obtained.

Furthermore, to enhance the comprehension of the electrochemical reaction kinetics for the N-BCFZYNF air electrode, EIS response curves and corresponding DRT plots under varying water partial pressure (pH_2O) and oxygen partial pressure (pO_2) were employed to provide additional insights into the individual elementary steps involved in the overall electrode reactions. Figure 5d displays the comparison fitted DRT plots for the N-BCFZYNF sample when the pH_2O increases from 3% to 10% in air, from which three separated peaks were observed and nearly kept no change with the different steam content in the operating atmosphere. This phenomenon suggests that the air electrode reaction kinetics will keep stable even under high steam content, which could be further demonstrated by the determined ASR values from the Nyquist profiles in air with different pH_2O (Figures 5e and S8, Supporting Information). The ASR value for N-BCFZYNF air electrode, at ≈0.165 Ω cm^2, is nearly stable, whereas those of BCFZY increase from the initial 0.264 to

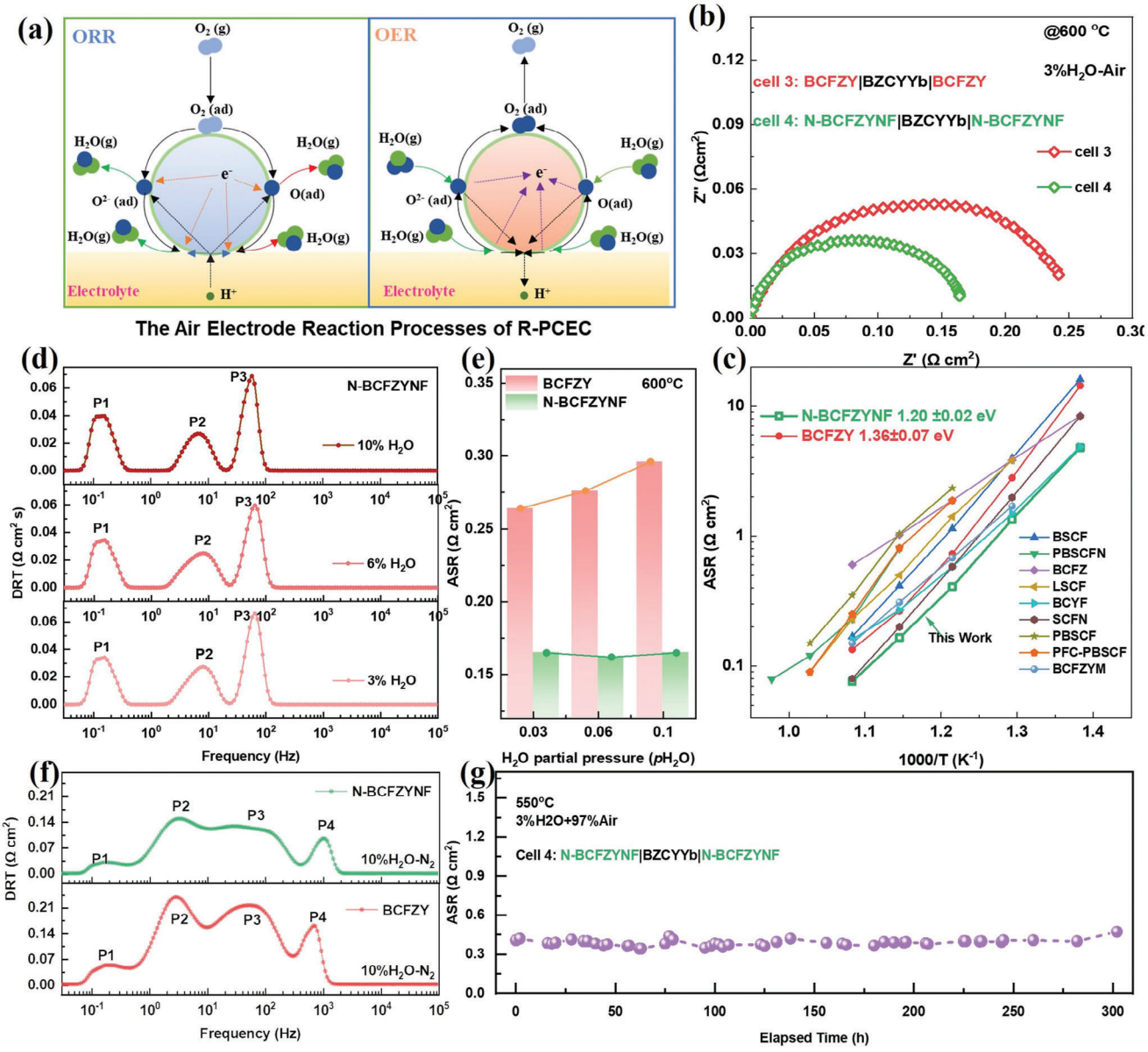

Figure 5. The electrocatalytic activity of BCFZY and N-BCFZYNF samples: a) schematic illustration of the ORR/OER processes for air electrodes; b) the Nyquist plots of symmetrical cell 3 and 4 at 600 °C in wet air; c) Arrhenius plots of ASR values as a function of temperature in wet air; d) the comparison of DRT plots for N-BCFZYNF sample in different pH_2O operating at 600 °C; e) the corresponding ASR values of both samples; f) the comparison DRT plots for various samples in high pH_2O (10%) without oxygen at 600 °C; g) the long-term ASR values of symmetrical cell 4 with N-BCFZYNF air electrode.

0.296 Ω cm^2 with the pH_2O lift from 3% to 10%. These contrasting trends observed in different air electrodes further highlight the efficient stability of the modified N-BCFZYNF electrode's electrocatalytic activity, which is likely attributed to the enhanced proton generation and conduction capabilities of N-BCFZYNF, compensating for the weaker oxygen ion transport characteristics under high water vapor pressure. Consequently, the electrode demonstrates overall stable electrocatalytic activity.

At the same time, the various pO_2 effects on the electrode reactions were also investigated, with the results shown in Figures S9 and S10, Supporting Information. It can be clearly seen from the DRT plots (Figure S9a, Supporting Information) that all peaks' enclosed area reduced with higher pO_2 in the operating atmosphere, which kept consistent with the overall ASR values (Figures S9b and S10, Supporting Information) dropping accordingly, similar results could also be found in some previous reports.[15,29,51] Analyzing both the peak locations (characteristic frequencies) and the acceleration features, P1 (LF) is likely associated with the oxygen gas diffusion process, P2 (IF) is linked to oxygen transfer within the electrode bulk, and Padd1 (IF) is probably connected with O^{2-} production since it minimized in abundant O_2 conditions. P3 (HF) may be related to the charge transfer process involved in ORR/OER. In summary, considering the influence of pH_2O and pO_2, the electrochemical processes

corresponding to characteristic peaks in the DRT plots and ASR values in Nyquist plots suggest that the modified N-BCFZYNF electrode can exhibit more stable and efficient ORR/OER catalytic activity in high vapor pressure and low oxygen partial pressure conditions.

To delve deeper into both electrodes' proton uptake and transport capabilities in humid atmosphere, ASRs and DRT plots were conducted in humid nitrogen, eliminating the influence of O_2 mass diffusion, oxygen-related surface exchange, and O^{2-} transfer processes. The DRT analysis results (Figures 5f and S11, Supporting Information) indicated a reduction in all peaks for the fluorinated BCFZY decorated by NiO nanoparticles, suggesting an enhancement in all related to proton-involved sub-steps of electrode reactions. By combining the peak locations and the analysis results presented in Figures 5d and S9a, Supporting Information, this improvement can be attributed to faster H_2O diffusion (P1, LF) and the rapid formation and transfer of hydroxide defects (P2, P3, IF), aligning with the stronger proton transfer ability mentioned in Figure 4. This illustrates that the outstanding formation and transfer of hydroxide defects of the N-BCFZYNF triple conducting oxide are highly valuable for R-PCECs air electrodes.

Above all, the EIS and DRT results collectively indicate that N-BCFZYNF exhibits superior electrocatalytic activity, and this excellent catalytic performance can be sustained over an extended period, as evidenced by the long-term stability of the symmetrical cell in humid air at 550 °C (Figure 5g). The assessed ASR values remained ≈0.407 Ω cm^2 without significant degradation during the 300h-operation in wet air, indicating remarkable durability of the N-BCFZYNF electrode on the BZCYYb proton-conducting electrolyte in a steam-containing atmosphere. With its efficient and stable electrocatalytic activity, this electrode is highly suitable for using as an air electrode in proton-conducting electrolyte cells.

To verify the superior ORR/OER catalytic performance of N-BCFZYNF under real fuel cell operating mode, the Ni-BZCYYb fuel electrode supported single cells with the pristine BCFZY and modified N-BCFZYNF air electrodes were fabricated and tested, respectively. **Figure** 6a presents the typic *i-V-p* polarization curves of the PCFC with BCFZY air electrode, fueled with pure hydrogen (H_2) and ambient air as the oxidant. It is evident that the peak power density (PPD) of this cell reached 626 mW cm^{-2} at 650 °C. Meanwhile, when the single cell utilized N-BCFZYNF as the air electrode (Figure 6b), its PPD value significantly increased to 996 mW cm^{-2} under the same test conditions, experiencing a ~60% enhancement. This improvement confirms the superior ORR catalytic activity of the fluorine-nickel-modified BCFZY electrode. Remarkably, as shown in Figure 6c and Table S4, Supporting Information, the rarely high PPDs achieved for the single cell based on N-BCFZYNF is also outperformed most of state-of-art air electrodes reported so far, suggesting the favorable potential of applying the N-BCFZYNF as the air electrode for actual application. The exceptional performance can be attributed to the enhanced kinetics of oxygen and proton transport and surface diffusion, resulting in accelerated ORR catalytic activity. This is further evidenced by the significantly lower ASR values, measuring only 0.06 and 0.13 Ω cm^2 under open-circuit voltage (OCV) conditions at 650 and 600 °C, respectively (Figure S12, Supporting Information). The presence of a dense electrolyte layer alongside an elevated OCV value serves as a compelling testament to the excellent R-PCEC sealing condition and a noteworthy mitigation of internal hydrogen leakage concerns, which further substantiates the credibility of the obtained results. To underscore the operational stability of the N-BCFZYNF air electrode, a long-term durability test of this single cell was conducted under a constant current density of 0.42 A cm^{-2} at 550 °C, with results shown in Figure 6d. It can be observed that the cell voltage exhibited negligible degradation, stabilizing at ~0.79–0.75 V during the 60-h operation.

Moreover, to validate the reversible ORR/OER electrocatalytic activities of the distinct air electrodes, equivalent single cells were prepared for electrochemical reversibility testing in the R-PCEC mode. As illustrated in Figures 6e,f, the obtained i–V curves of R-PCECs with the unmodified BCFZY air electrode and the corresponding N-BCFZYNF-modified air electrodes both exhibited excellent reversibility between the fuel cell (FC) mode and electrolysis cell (EC) mode by supplying pure H_2 and 3% H_2O-air to the fuel and air electrodes, respectively. Notably, the electrolysis current density for the BCFZY electrode reached 886, 527, 317, and 148 mA cm^{-2} at temperatures of 650, 600, 550, and 500 °C, respectively, when the applied voltage was 1.3 V. Conversely, those of the N-BCFZYNF electrode sharply increased to 1570, 1089, 684, and 354 mA cm^{-2}, indicating the fluorine-nickel-modified BCFZY electrode's more active OER catalytic performance. Moreover, its electrochemical performance nearly keeps stable with increasing water vapor pressure (up to 20%), indicating that the partial pressure of H_2O has no significant impact on cell performance (Figure S14, Supporting Information). Additionally, this remarkable electrolysis performance surpassed many reported state-of-the-art air electrodes assembled in R-PCECs (Figure 6g and Table S5, Supporting Information). Furthermore, as depicted in Figure 6h, an electrolysis operational stability test for this cell in EC mode was conducted at 550 °C. It was observed that the electrolysis performance of N-BCFZYNF remained stable without significant degradation under a constant high electrolysis current density of −0.50 A cm^{-2}, further demonstrating the superiority of the N-BCFZYNF electrode. Simultaneously, the inset SEM image and results shown in Figure S13, Supporting Information also confirmed that the N-BCFZYNF air electrode maintained good contact with the electrolyte film without any breaks or delamination after the durability test, indicating the favorable thermal expansion coefficient matching and thermal stability properties of these layers. The Faradaic efficiency (FE) and hydrogen (H_2) production rate of the cell were evaluated at 550 °C under atmospheric conditions containing 20 vol% vapor in air. Specifically, the FE reached ≈83% (Figure S16, Supporting Information) at an electrolysis current density of −500 mA cm^{-2}, which further underscores the significant potential of the N-BCFZYNF air electrode for water splitting in R-PCECs.

More importantly, a good reversibility feasibility of R-PCEC with this advanced N-BCFZYNF air electrode should also be emphasized for practical application. The cell reversibility was evaluated by cyclic switching between the hydrogen production (−0.50 A cm^{-2}) and power generation modes (0.38 A cm^{-2}) under varying current density conditions at 550 °C, with the results shown in Figure 6i. It can be intuitively seen that the R-PCEC has run stably throughout 15 reversible cycles within 100 h without appreciable performance degradation. Notably, the electrode material exhibits a consistent amalgamation of nanoscale particles

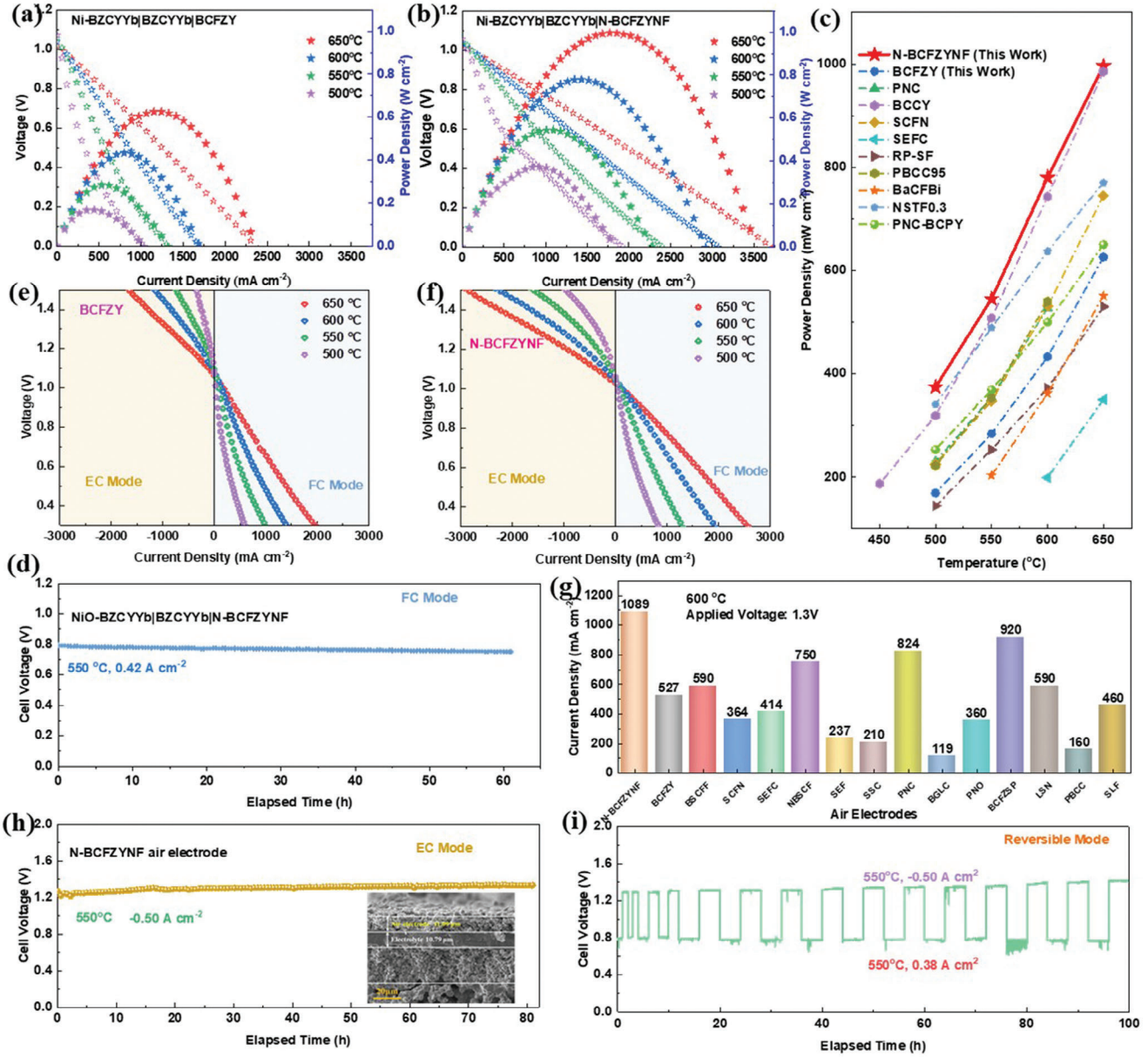

Figure 6. The electrochemical performance of R-PCEC with BCFZY and N-BCFZYNF air electrodes: the comparison *i–V–p* curves of the Ni-BZCYYb supported PCFCs with a) the pristine BCFZY electrode and b) N-BCFZYNF electrode at 500-650 °C; c) the PPD values of PCFCs fabricated by different air electrodes (this work and other reported ones); d) durability of single cell with targeted N-BCFZYNF air electrode at 550 °C with a constant output current density of 0.42 A cm^{-2}; the *i–V* curves of R-PCEC operated at both fuel cell and electrolysis modes at 500–650 °C with e) BCFZY and f) N-BCFZYNF air electrodes; g) the electrolysis current density comparison of R-PCEC at 1.3 V with various air electrodes; h) the stability of R-PCEC operated in electrolysis mode at 550 °C; i) tthehe durability of continuous R-PCEC operation, cycling between electrolysis and fuel cell modes at 550 °C.

and primary phase material after long-term testing (Figure S15, Supporting Information), which further provides partial insight into the favorable stability demonstrated by the R-PCEC configuration incorporating the novel N-BCFZYNF air electrode. The reliable conversion operational capability at different current densities strongly revealed that N-BCFZYNF air electrode has good durability and chemical stability, as well as excellent adhesion and compatibility with the electrolyte. These findings suggest that the N-BCFZYNF holds promise as a potential air electrode material for R-PCEC with highly appreciated activity and durability.

3. Conclusion

This work successfully synthesized a novel bifunctional air electrode material (N-BCFZYNF) by concurrently modifying bulk-phase metal-oxygen bonds and in-situ surface formation of metal oxide nano-catalysts. The physicochemical properties of this electrode material are systematically investigated, and all results reveal that the synergistic optimization effects at both bulk and surface modifications significantly enhance the electrochemical environment for interactions involving oxygen and

protons, which manifest in substantially improved oxygen adsorption/desorption and hydration rates, as well as enhanced capabilities for oxygen ion and proton transport in both surface and bulk. Such improvements are deemed favorable for optimizing electrode kinetics. Therefore, the sluggish ORR/OER kinetics of the parent BCFZY air electrode are significantly accelerated, ensuring the excellent electrochemical performance of the N-BCFZYNF catalyst in FC and EC modes. Specifically, the peak power density operating in FC mode reached 996 mW cm^{-2} at 650 °C, and the electrolysis current density in EC mode reached a remarkably high value of 1570 mA cm^{-2} at an applied voltage of 1.3 V. The cyclic operation of power generation and hydrogen production under different current densities further demonstrated the high adaptability and durability of the N-BCFZYNF catalyst when assembled as the R-PCEC air electrode. This approach, simultaneously optimizing the bulk M—O chemical bonds and surface-modified MO nano-catalysts in the perovskite oxide air electrode, provides a design strategy aimed at improving the electrochemical performance of TCO materials. Moreover, it still holds significance for the exploration of catalysts in other electrochemical systems.

Supporting Information

Supporting Information is available from the Wiley Online Library or from the author.

Acknowledgements

M.N. thanks the grants (Project Number: 15306723 and SRFS2324-5S02) from Research Grants Council, University Grants Committee, Hong Kong SAR. and National Nature Science Foundation of China (22209138), Guangdong Basic and Applied Basic Research Foundation (2021A1515110464). F.C. gratefully acknowledges the Research Grant Council of Hong Kong for support through the projects (16201820 and 16201622). This work was partly supported by the Project of Hetao Shenzhen-Hong Kong Science and Technology Innovation Cooperation Zone (HZQB-KCZYB-2020083, received by F.C.). The authors extend their gratitude to Shiyanjia Lab (www.shiyanjia.com) for providing assistance with the XPS test.

Conflict of Interest

The authors declare no conflict of interest.

Data Availability Statement

The data that support the findings of this study are available from the corresponding author upon reasonable request.

Keywords

air electrode, metal oxide nano-catalyst, metal-oxygen bonds, oxygen reduction/evolution reactions, reversible protonic ceramic electrochemical cells

Received: March 18, 2024
Revised: May 22, 2024
Published online: June 4, 2024

[1] I. Cho, J. Yun, B. Seong, J. Kim, S. H. Choi, H.-I. Ji, S. Choi, *J. Energy Chem.* **2024**, *88*, 1.
[2] S. Fankhauser, S. M. Smith, M. Allen, K. Axelsson, T. Hale, C. Hepburn, J. M. Kendall, R. Khosla, J. Lezaun, E. Mitchell-Larson, M. Obersteiner, L. Rajamani, R. Rickaby, N. Seddon, T. Wetzer, *Nat. Clim. Chang.* **2022**, *12*, 15.
[3] S. Zhao, T. Liu, Y. Dai, J. Wang, Y. Wang, Z. Guo, J. Yu, I. T. Bello, M. Ni, *Appl. Catal. B* **2023**, *320*, 121992.
[4] J. H. Kim, D. Kim, S. Ahn, K. J. Kim, S. Jeon, D.-K. Lim, J. K. Kim, U. Kim, H.-N. Im, B. Koo, K. T. Lee, W. Jung, *Energy Environ. Sci.* **2023**, *16*, 3803.
[5] A. Hauch, R. Küngas, P. Blennow, A. B. Hansen, J. B. Hansen, B. V. Mathiesen, M. B. Mogensen, *Science* **2020**, *370*, eaba6118.
[6] F. He, M. Hou, F. Zhu, D. Liu, H. Zhang, F. Yu, Y. Zhou, Y. Ding, M. Liu, Y. Chen, *Adv. Energy Mater.* **2022**, *12*, 2202175.
[7] C. Zhou, X. Wang, D. Liu, M. Fei, J. Dai, D. Guan, Z. Hu, L. Zhang, Y. Wang, W. Wang, R. O'Hayre, S. P. Jiang, W. Zhou, M. Liu, Z. Shao, *Energy Environ. Mater.* **2023**, *0*, e12660.
[8] D. Kim, K. T. Bae, K. J. Kim, H.-N. Im, S. Jang, S. Oh, S. W. Lee, T. H. Shin, K. T. Lee, *ACS Energy Lett.* **2022**, *7*, 2393.
[9] F. Liu, H. Deng, D. Diercks, P. Kumar, M. H. A. Jabbar, C. Gumeci, Y. Furuya, N. Dale, T. Oku, M. Usuda, P. Kazempoor, L. Fang, D. Chen, B. Liu, C. Duan, *Nat. Energy* **2023**, *8*, 1145.
[10] X. Wang, W. Li, C. Zhou, M. Xu, Z. Hu, C.-W. Pao, W. Zhou, Z. Shao, *ACS Appl. Mater. Interfaces* **2023**, *15*, 1339.
[11] C. Duan, R. Kee, H. Zhu, N. Sullivan, L. Zhu, L. Bian, D. Jennings, R. O'Hayre, *Nat. Energy* **2019**, *4*, 230.
[12] P. Qiu, B. Liu, L. Wu, H. Qi, B. Tu, J. Li, L. Jia, *J. Adv. Ceram.* **2022**, *11*, 1988.
[13] X. Xu, H. Wang, M. Fronzi, X. Wang, L. Bi, E. Traversa, *J. Mater. Chem. A* **2019**, *7*, 20624.
[14] Y. Zhang, X. Hao, J. Liu, X. Yang, H. Xu, Z. Wang, Y. Luo, F. Wang, T. He, *Ceram. Int.* **2024**, *50*, 4746.
[15] Z. Liu, D. Cheng, Y. Zhu, M. Liang, M. Yang, G. Yang, R. Ran, W. Wang, W. Zhou, Z. Shao, *Chem. Eng. J.* **2022**, *450*, 138153.
[16] M. Liang, Y. Song, D. Liu, L. Xu, M. Xu, G. Yang, W. Wang, W. Zhou, R. Ran, Z. Shao, *Appl. Catal. B* **2022**, *318*, 121868.
[17] Y. Xu, K. Xu, F. Zhu, F. He, H. Zhang, C. Fang, Y. Liu, Y. Zhou, Y. Choi, Y. Chen, *ACS Energy Lett.* **2023**, *8*, 4145.
[18] R. Zohourian, R. Merkle, G. Raimondi, J. Maier, *Adv. Funct. Mater.* **2018**, *28*, 1801241.
[19] N. Wang, C. Tang, L. Du, R. Zhu, L. Xing, Z. Song, B. Yuan, L. Zhao, Y. Aoki, S. Ye, *Adv. Energy Mater.* **2022**, *12*, 2201882.
[20] Z. Wang, Y. Wang, J. Wang, Y. Song, M. J. Robson, A. Seong, M. Yang, Z. Zhang, A. Belotti, J. Liu, G. Kim, J. Lim, Z. Shao, F. Ciucci, *Nat. Catal.* **2022**, *5*, 777.
[21] L. Zhang, W. Sun, C. Xu, R. Ren, X. Yang, J. Qiao, Z. Wang, K. Sun, *J. Mater. Chem. A* **2020**, *8*, 14091.
[22] C. Yang, Y. Tian, C. Yang, G. Kim, J. Pu, B. Chi, *Adv. Sci.* **2023**, *10*, 2304224.
[23] T. Hu, F. He, M. Liu, Y. Chen, *Prog. Mater. Sci.* **2023**, *133*, 101050.
[24] X. Li, Z. Chen, D. Huan, B. Qiu, K. Zhu, Z. Qi, H. Liu, C. Xia, R. Peng, Y. Lu, *ACS Mater. Lett.* **2023**, *5*, 2896.
[25] Y. Zhou, W. Zhang, N. Kane, Z. Luo, K. Pei, K. Sasaki, Y. Choi, Y. Chen, D. Ding, M. Liu, *Adv. Funct. Mater.* **2021**, *31*, 2105386.
[26] K. Pei, S. Luo, F. He, J. Arbiol, Y. Xu, F. Zhu, Y. Wang, Y. Chen, *Appl. Catal. B* **2023**, *330*, 122601.
[27] W. Zhang, H. Muroyama, Y. Mikami, T. Matsui, K. Eguchi, *J. Energy Chem* **2023**, *87*, 450.
[28] J. H. Kim, J. K. Kim, J. Liu, A. Curcio, J.-S. Jang, I.-D. Kim, F. Ciucci, W. Jung, *ACS Nano* **2021**, *15*, 81.
[29] F. Zhu, F. He, D. Liu, H. Zhang, Y. Xu, K. Xu, Y. Chen, *Energy Storage Mater.* **2022**, *53*, 754.

[30] Y. Zhou, E. Liu, Y. Chen, Y. Liu, L. Zhang, W. Zhang, Z. Luo, N. Kane, B. Zhao, L. Soule, Y. Niu, Y. Ding, H. Ding, D. Ding, M. Liu, *ACS Energy Lett.* **2021**, *6*, 1511.
[31] T. Hu, F. Zhu, J. Xia, F. He, Z. Du, Y. Zhou, Y. Liu, H. Wang, Y. Chen, *Adv. Funct. Mater.* **2023**, *33*, 2305567.
[32] M. Liang, Y. Wang, Y. Song, D. Guan, J. Wu, P. Chen, A. Maradesa, M. Xu, G. Yang, W. Zhou, W. Wang, R. Ran, F. Ciucci, Z. Shao, *Appl. Catal. B* **2023**, *331*, 122682.
[33] M. Liang, Y. Zhu, Y. Song, D. Guan, Z. Luo, G. Yang, S. P. Jiang, W. Zhou, R. Ran, Z. Shao, *Adv. Mater.* **2022**, *34*, 2106379.
[34] S. Joo, A. Seong, O. Kwon, K. Kim, J. H. Lee, R. J. Gorte, J. M. Vohs, J. W. Han, G. J. S. Kim, *Sci. Adv.* **2020**, *6*, eabb1573.
[35] S. Joo, O. Kwon, K. Kim, S. Kim, H. Kim, J. Shin, H. Y. Jeong, S. Sengodan, J. W. Han, G. Kim, *Nat. Commun.* **2019**, *10*, 697.
[36] J. Xiong, H. Zhong, J. Li, X. Zhang, J. Shi, W. Cai, K. Qu, C. Zhu, Z. Yang, S. P. Beckman, H. Cheng, *Appl. Catal. B* **2019**, *256*, 117817.
[37] Y. Xie, N. Shi, D. Huan, W. Tan, J. Zhu, X. Zheng, H. Pan, R. Peng, C. Xia, *ChemSusChem* **2018**, *11*, 3423.
[38] P. Anitha Sukkurji, A. Molinari, C. Reitz, R. Witte, C. Kübel, V. S. K. Chakravadhanula, R. Kruk, O. Clemens, *Materials* **2018**, *11*, 1204.
[39] J. Zhu, G. Liu, Z. Liu, Z. Chu, W. Jin, N. Xu, *Adv. Mater.* **2016**, *28*, 3511.
[40] W. Wang, X. Zhang, D. Zhang, Q. Zeng, Y. Jiang, B. Lin, *Ceram. Int.* **2020**, *46*, 23964.
[41] D. Huan, L. Zhang, X. Li, Y. Xie, N. Shi, S. Xue, C. Xia, R. Peng, Y. Lu, *ChemSusChem* **2020**, *13*, 4994.
[42] X. Ding, Z. Gao, D. Ding, X. Zhao, H. Hou, S. Zhang, G. Yuan, *Appl. Catal. B* **2019**, *243*, 546.
[43] Y. Shin, K.-Y. Doh, S. H. Kim, J. H. Lee, H. Bae, S.-J. Song, D. Lee, *J. Mater. Chem. A* **2020**, *8*, 4784.
[44] M. B. Effat, E. Quattrocchi, T. H. Wan, M. Saccoccio, A. Belotti, F. Ciucci, *J. Electrochem. Soc.* **2017**, *164*, F1671.
[45] D. Chen, Z. Shao, *Int. J. Hydrogen Energy* **2011**, *36*, 6948.
[46] R. Ren, X. Yu, Z. Wang, C. Xu, T. Song, W. Sun, J. Qiao, K. Sun, *Appl. Catal. B* **2022**, *317*, 121759.
[47] X. Chen, N. Yu, I. T. Bello, D. Guan, Z. Li, T. Liu, T. Liu, Z. Shao, M. Ni, *Energy Storage Mater.* **2023**, *63*, 103056.
[48] A. B. Muñoz-García, A. M. Ritzmann, M. Pavone, J. A. Keith, E. A. Carter, *Acc. Chem. Res.* **2014**, *47*, 3340.
[49] J. Hou, J. Qian, L. Bi, Z. Gong, R. Peng, W. Liu, *J. Mater. Chem. A* **2015**, *3*, 2207.
[50] T. H. Wan, M. Saccoccio, C. Chen, F. Ciucci, *Electrochim. Acta* **2015**, *184*, 483.
[51] Y. Niu, Y. Zhou, W. Zhang, Y. Zhang, C. Evans, Z. Luo, N. Kane, Y. Ding, Y. Chen, X. Guo, W. Lv, M. Liu, *Adv. Energy Mater.* **2022**, *12*, 2103783.